

The formation of methanol from glycerol bio-waste over doped ceria based catalysts

Jay Devlia, Louise Smith, Mark Douthwaite, Stuart H. Taylor, David J. Willock, Graham J. Hutchings and Nicholas F. Dummer

Cardiff Catalysis Institute, School of Chemistry, Cardiff University, Main Building, Park Place, Cardiff, CF10 3AT, UK. NFD, 0000-0002-0946-6304

Keywords: Glycerol, methanol, ceria, dopant, praseodymium, zirconia

Summary

A series of ceria-based solid-solution metal oxides were prepared by co-precipitation and evaluated as catalysts for glycerol cleavage, principally to methanol. The catalyst activity and selectivity to methanol were investigated with respect to the reducibility of the catalysts. Oxides comprising of Ce-Pr and Ce-Zr were prepared, calcined and compared to CeO₂, Pr₆O₁₁ and ZrO₂. The oxygen storage capacity of the catalysts was examined with analysis of Raman spectroscopic measurements and a temperature programmed reduction, oxidation and reduction cycle. The incorporation of Pr resulted in significant defects, as evidenced by Raman spectroscopy. The materials were evaluated as catalysts for the glycerol to methanol reaction and it was found that an increased defect density or reducibility was beneficial. The space time yield of methanol normalised to surface area over CeO₂ was found to be 0.052 mmol_{MeOH} m⁻² h⁻¹ and over CeZrO₂ and CePrO₂ this was to 0.029 and 0.076 mmol_{MeOH} m⁻² h⁻¹ respectively. The inclusion of Pr reduced the surface area, however, the carbon mole selectivity to methanol and ethylene glycol remained relatively high, suggesting a shift in the reaction pathway compared to that over ceria. This article is part of a discussion meeting issue "Science to enable the circular economy".

1. Introduction

The increased research and development in sustainable routes to valuable chemicals, largely derived from bio-based feedstock continues unabated. Increased adoption of biodiesel as a fuel blend has been one area of intensive development, however, a number of other processes have been investigated, such as the production of bio-alcohols [1-3]. The formation of bio-diesel via transesterification of triglycerides with methanol results in the formation of impure glycerol [4]. Utilisation of this glycerol, in its crude form as a chemical feedstock is challenging and presently it can be used in anaerobic digestion to produce methane. However, following purification glycerol is a high value product and can be used in a diverse range of industries, such as pharmaceuticals and food. Additionally, reports have emerged detailing oxidation, dehydration and hydrogenation of purified glycerol [5-11].

Recently, we reported on the cleavage of glycerol to methanol, and a mixture of other compounds, using MgO and CeO₂ catalysts [12-14]. To optimise the yield of methanol over the catalyst we began systematically

*Author for correspondence Nicholas F. Dummer (dummernf@cardiff.ac.uk).

†Present address: Cardiff Catalysis Institute, Cardiff University, Cardiff, CF10 3AT, UK

investigating aspects of the catalysts that could increase selective reactions. The reducibility or oxygen storage capacity of CeO₂ has been noted in relation to water gas shift catalysts and automotive exhaust technologies. Herein, we report our efforts to rationalise the use of dopants to enhance catalyst activity with several ceria-based catalysts. The ability of ceria to release oxygen under a reducing atmosphere is well known and is a key factor in its use as a catalyst for the water-gas shift reaction [15] and for automotive exhaust treatment [16]. For example, oxygen can be replaced through absorption under oxidising conditions and this reversible process is key to its success as a catalyst provided the cubic fluorite structure is maintained. Furthermore, relatively high surface areas and small particle sizes are crucial to enhance the oxygen storage capacity (OSC) and reducibility of ceria.

Solid solutions of ceria, as Ce_{1-x}M_xO_{2-δ} with another metal ions such as Zr⁴⁺ [17, 18], Hf⁴⁺ [19], Eu³⁺ [20], Pr^{3+/4+} [19, 21], Sm³⁺ [22] or La³⁺ [23] have been used to further enhance or stabilise the OSC of this class of catalysts [24] and the ratio of Ce³⁺ to Ce⁴⁺. The inclusion of Zr⁴⁺ ions can significantly enhance the reducibility of Ce⁴⁺ in a solid solution [25, 26], although, the density of oxygen vacancies was not increased as a result. However, the thermal stability of the solid solution is improved and the defects present are maintained with the incorporation of Zr [27].

The incorporation of certain metal ions within the cubic fluorite structure can improve the OSC as with La³⁺ [23] and Ce_xPr_{1-x}O_{2x} [21] through the creation of defect sites. Notably, this can be observed by examination of the mixed-metal oxides with Raman spectroscopy. The dominant mode observed at ca. 460 cm⁻¹ for CeO₂, described as the F_{2g} mode, can shift to lower frequencies when Eu or Pr are added. This shift has been ascribed to the greater atomic mass of these elements, however, in this vibration only the oxygen atoms move. The mode frequency should be independent of the cation mass, other factors such as phono confinement, strain and inhomogeneity of the distribution of cation radii contribute to the shift and line width of the F_{2g} mode [20].

Potentially, the valorisation of waste glycerol to methanol can be used in the formation of bio-diesel. At present the methanol used in the bio-diesel is a non-renewable component in the production chain of a sustainable fuel.

2. Experimental

2.1 Materials

Cerium(III) nitrate hexahydrate (99.9% trace metals basis), praseodymium(III) nitrate hexahydrate (99.9% trace metals basis) and the other with zirconium(IV) oxynitrate hydrate (≥99.0% trace metals basis) and glycerol (99%) were procured from Sigma-Aldrich (now Merck) and used as received. Argon gas was purchased from BOC (Guildford, UK). Deionised (DI) water was provided in-house. Silicon carbide (SiC, 98 %, Alfa Aesar, Ward Hill, MA, USA) of 40–50 mesh size was washed (DI water) and dried prior to use.

2.2 Catalyst Preparation

Single and mixed-metal oxide catalysts were prepared using a co-precipitation technique. In both cases the metal nitrate (3 mmol) was dissolved in 50 mL of deionized water and added to pre-heated deionized water under vigorous stirring (total 300 mL at 80 °C). The pH of the solution was monitored and an ammonium hydroxide solution (1 M) was added dropwise until the pH reached 9. At this point, the slurry was immediately filtered and subsequently washed with warm DI water (500 mL) and then ethanol (200 mL). The recovered solid was dried at 120 °C for 16 h and then calcined at 500 °C for 5 h under static air.

2.3 Catalyst Testing

Catalytic reactions were carried out using a gas-phase micro-reactor operating under continuous flow. Aqueous solutions containing glycerol (50 wt. %) were fed using a HPLC pump at a flow rates of 0.016 mL min⁻¹ into a preheater and vaporised (305 °C). The glycerol vapour was passed through the reactor using a carrier gas; argon (15–45 mL min⁻¹). The reactor lines were heated to 300 °C (pre-catalyst bed) and 110 °C (post-catalyst bed) to prevent condensation of feedstock or reaction products. Catalysts were used with a uniform particle size (250–425 μm), formed through pelleting, crushing and finally sieving. Typically, the catalyst samples (0.5 g) were diluted with silicon carbide to a uniform volume (2 mL) and placed into a stainless-steel tube with an 8 mm inner diameter supported by quartz wool, above and below the bed. These conditions resulted in mass velocities and space velocities between 600 L h⁻¹Ar kg⁻¹cat. and 545-950 L h⁻¹Ar L⁻¹cat. respectively. A thermocouple was

placed in the catalyst bed and used to control the reaction temperature, at 360 °C. The flow of aqueous glycerol was passed over the catalysts bed for 135 minutes prior to product collection to allow the reaction-feed to achieve a steady flow. Reaction products (liquids) were collected using a stainless-steel trap (held at *ca.* 0 °C). Gaseous products were collected in a gas bag that was attached to the exit line of the liquid trap.

Analysis of liquid reaction products were performed offline using a CP 3800 gas chromatograph (GC1, Varian now Agilent Technologies, Santa Clara, CA, US; capillary column; ZB-Wax plus, 30 m × 0.53 mm × 1 µm). An external standard (cyclohexanol) was used. Gaseous, carbon-based reaction products were analysed offline using a Varian 450-GC gas chromatograph (GC2; capillary column; CP-Sil5CB, 50 m × 0.32 mm × 5 µm). Non-carbon-based gases; H₂ and O₂ were analysed using a Varian CP3380 gas chromatograph (GC3; Porapak Q column). Gaseous products were calibrated using gas mixtures of the product with a known concentration, with an inert gas (Ar). Product selectivities (carbon mol. %) were calculated from the moles of carbon in a product recovered divided by the total moles of carbon in all products. Product list and retention times based on GC analysis are illustrated in Table S1.

2.4 Calculations

The glycerol conversion (C_{GLY}) was calculated according to Equation (1) and based on the molar difference between carbon from glycerol fed into the reactor, g_{mi} , and that detected at the outlet, g_{mo} :

$$C_{GLY} (\%) = \left(\frac{g_{mi} - g_{mo}}{g_{mi}} \right) \times 100 \quad (1)$$

The product selectivity ($S_p(x)$, carbon mol. %) for any product, x , was calculated from the moles of carbon recovered in x , x_{cm} divided by the sum of moles of carbon in each product, y_{cm} (Equation (2)):

$$S_p(x)(\%) = \left(\frac{x_{cm}}{\sum_y y_{cm}} \right) \times 100 \quad (2)$$

The carbon balance can be obtained by comparing the moles of carbon accounted for in unreacted glycerol and in the identified products to the moles of carbon in glycerol entering the reactor:

$$B_C(\%) = \left(\frac{g_{mo} + \sum_x x_{cm}}{g_{mi}} \right) \times 100 \quad (3)$$

The intrinsic activity of the catalyst $IA_{Catalyst}$, was calculated (Equation (4)) from the mass of methanol m_{MEOH} , produced per h (reaction time Rt), per mass of catalyst (m_{cat} , kg):

$$IA_{Catalyst} = \left(\frac{m_{MEOH} (g)}{Rt (h) \times m_{cat} (kg)} \right) \quad (4)$$

The specific activity of the catalyst $SA_{Catalyst}$, was calculated (Equation (5)) from the mass of methanol m_{MEOH} , produced per h (reaction time Rt), per surface area of catalyst ($Area_{cat}$, m² g⁻¹):

$$SA_{Catalyst} = \left(\frac{m_{MEOH} (g)}{Rt (h) \times Area_{cat} (m^2 g^{-1})} \right) \quad (5)$$

2.5 Characterisation

Powder X-ray diffraction (XRD) analysis of the catalysts was carried out on a PANalytical X'pert Pro powder diffractometer (Malvern Panalytical, Malvern, UK) using a Cu source operated at 40 KeV and 40 mA with a Ge (111) monochromator to select K_{α1} X-rays. Patterns were analysed from measurements taken over the 2θ angular range 10–80° (step size of 0.016°).

Surface area analysis was carried out using the Brunauer Emmett Teller (BET) method with a Gemini VII 2390 Surface Area Analyzer (Micromimetics, Norcross, GA, USA). A five point analysis was carried out using an adsorbate gas (N₂ at –196 °C). Samples (100 mg) were degassed under vacuum for 3 h at 110 °C prior to analysis.

Raman spectroscopy was performed using an inVia microscope (Renishaw, Gloucestershire, UK) operated at a wavelength of 514 nm. 10 acquisitions were performed per sample with an exposure time of 10 s; the laser was employed at 1% power.

The reducibility of each material was probed by conducting a series of monitored temperature programmed thermal treatments, conducted using a Quantachrome ChemBET Chemisorption analyser. In a typical experiment, the material was first heated to 130 °C (15 °C min⁻¹) under He (30 mL min⁻¹). After cooling, the material was then reduced at 900 °C (15 °C min⁻¹) under 5 % H₂/He (30 mL min⁻¹). Once cooled, the material is subsequently oxidised to 900 °C (15 °C min⁻¹) under 10 % O₂/He (30 mL min⁻¹). After cooling one final time, the material was reduced once again at 900 °C (15 °C min⁻¹) under 5 % H₂/He (30 mL min⁻¹). The consumption of H₂ was monitored using a thermal conductivity detector and quantified using an external calibration with a CuO standard.

Scanning electron microscopy (SEM-EDX) was performed on a Tescan Maia3 (Tescan Orsay Holding, a.s., Czech Republic) field emission gun fitted (FEG-SEM) with an Oxford Instruments XMAXN 80. Images were acquired using the secondary electron (SE) detector. Samples were dispersed as a powder onto adhesive carbon Leit discs mounted onto aluminium stubs.

3. Results and Discussion

3.1 Catalyst Characterisation

Two sets of ceria-based samples were prepared via a co-precipitation route; one set utilized Pr(NO₃)₃·6H₂O as a precursor and the other, ZrO(NO₃)₂·H₂O in various ratios. The sample designators are displayed in Table 1. These samples were characterised with nitrogen adsorption, powder XRD, Raman spectroscopy, temperature programmed reduction/oxidation cycles and SEM-EDX. The chemical composition of the Ce-M-O samples was explored by SEM-EDX and compared to the theoretical composition used for preparation. In the two examples of mixed metal oxides prepared, Ce₃MOx and CeMOx the Ce to M ratio of 3:1 and 1:1 was used. The SEM-EDX surveys indicated that the Ce:M ratios varied from the intended values. In the case of the Ce:Zr samples the ratios were 7.6:1 and 1.1:1, whereas, in the case of the CePrOx samples the ratios were 1.9 and 0.6:1 respectively. It is possible that the pH used, which had been optimised for the synthesis of CeO₂, or short ageing time used to precipitate the samples may have contributed to the offset of the Ce:M ratios observed.

The BET surface areas of the samples are also presented in Table 1. These indicate that the combination of other metals to the standard ceria preparation led to increased surface areas of 88 and 106 m² g⁻¹ for the calcined Ce₃ZrOx (sample **B**) and CeZrOx (**C**) respectively, compared to 56 m²/g for CeO₂ (sample **A**). However, in the case of the Ce-Pr oxides the respective surface areas were increased to 75 m²/g for Ce₃PrOx (sample **E**) and reduced to 28 m² g⁻¹ for CePrOx (**F**).

The X-ray diffraction patterns of the samples are illustrated in Figure 1. From these data the crystallite size, lattice dimensions and cell volume were calculated (Table 1). The powder XRD of the samples was carried out to confirm phase purity and ensure that the catalysts retained the cubic fluorite structure of CeO₂ (Fig. 1). The peak positions of sample **A** closely matched the cubic space group of *Fm3m* (JCPDS no. 340394). Reflections at 28.5, 33.0, 47.4 and 56.2 degrees 2θ can be respectively assigned to the planes (111), (200), (220) and (311). The lattice parameter of 5.42 Å was close to the standard value of 5.41 Å reported for bulk ceria [28]. This modest increase can be ascribed to the relatively low calcination temperature of 500 °C. The space group of sample **D** was that of tetragonal zirconia in *P4₂/nmc* (JCPDS no. 50-1089), as expected from the calcination conditions [29]. Broad reflections at degrees 2θ of 30.2, 35.2, 50.4 and 60.0 can be assigned to (111), (200), (202) and (311) planes respectively. The minor shoulder at 28.7 degrees 2θ is likely evidence that a small proportion of monoclinic ZrO₂ phase existed in this sample [30].

Samples **B**, **C**, **E** and **F** were also found to possess the cubic fluorite lattice structure, however, sample **C** and to some extent **B**, exhibit peak broadening. This broadening is most likely due to dilution of the cubic ceria lattice with the smaller Zr ion (Zr⁴⁺ 0.84 Å), resulting in a reduction in crystallinity rather than the introduction of a binary tetragonal phase. Furthermore, the cell volume was found to be slightly lower in the CeZr oxides (*ca.* 157 Å³) compared to sample **A** of 159 Å³ (Table 1). The crystallite size was reduced with the inclusion of Zr into the

lattice, as estimated with the Scherrer equation from the (111) reflection (Table 1). Where the Ce to Zr ratio is approximately equivalent (sample C) the crystallite size was calculated to be ca. 7 nm compared to 13 nm for sample A.

The inclusion of Pr into the Ce lattice resulted in materials with lower crystallite sizes of ca. 8 nm (Table 1). However, in the case of sample E, the cell volume increased to 160 Å³ compared to sample A, suggesting a greater incorporation of Pr³⁺ (1.13 Å) into the lattice. Further, incorporation of Pr, as with sample F resulted in a reduction of the cell volume to 158 Å³ and suggests that Pr is largely present as Pr⁴⁺ as this has a slightly smaller ionic radii of 0.96 Å in a ratio of 1.7 Pr to 1 Ce. There is a modest expansion of the lattice parameter for sample G, which was found to be 5.47 Å compared to CeO₂ (A). The diffraction peak position with respect to 2θ, of both samples A and G are close, due to the similarity of their ionic radii; Ce⁴⁺ is 0.97 Å and Pr⁴⁺ is 0.96 Å. Due to the calcination temperature of 500 °C the composition of sample G is likely to be Pr₆O₁₁.

Raman spectra for all samples were obtained (Fig. 2) and all Ce-based samples possessed a large Raman mode centred at ca. 465 cm⁻¹. This mode describes the symmetric breathing (F_{2g} symmetry) of the O atoms around the cation and should be independent of the mass of this ion [28]. For samples with Zr incorporated into the lattice (B and C) there is a very minor shift of this dominant Raman mode from 462 cm⁻¹ found with sample A to 463 cm⁻¹ (Fig. 3a). The intensity of this mode increases with increasing Zr incorporation. The incorporation of Zr⁴⁺ into the ceria lattice is known to increase the reducibility of ceria and intrinsic oxygen vacancies form [19], however, this does not appear to occur.

Upon incorporation of Pr (Fig. 2b) the F_{2g} mode at ca. 462 cm⁻¹ for pure CeO₂ (A) shifts significantly to 450 cm⁻¹ for sample E and to 441 cm⁻¹ for sample F. This has been observed previously [28, 31] and was ascribed to the increased atomic mass of Pr in the lattice. The emergence of a broad mode centred at ca. 565 cm⁻¹ is commonly ascribed to oxygen vacancies in the lattice [28, 32, 33]. With increasing concentration of Pr in the lattice the relative intensity of the F_{2g} mode and the mode at 565 cm⁻¹ grow closer. The increasing proportion of oxygen vacancies as the Pr concentration increases has been observed previously and is attributed to substitution by Pr³⁺ ions into the lattice [33]. The integrated peak area percentage of the F_{2g} to defect mode was found to be 0.5 % for sample A and for the CeZrOx samples; ca. 0.8 %. For the CePrOx samples this increased significantly to 24 % for sample E and 49 % for sample F. In the case of samples B and C, the consistent proportion of the 463 to 565 cm⁻¹ modes suggests that oxygen vacancies are not present in B and C. The FWHM of the mode at 460 has been reported to be inversely related to the crystallite size and can be indicative of the presence of oxygen defects [34]. In the case of samples A, B and C this crystallite sizes decreased from 13 to 9 and then 7 nm respectively. The respective FWHM of the peaks as illustrated in Figure 3 are 18.6, 20.9 and 21.3 cm⁻¹, which suggests that the samples have comparable oxygen defect densities.

The reducibility of samples A, E, F and G were investigated to gain an understanding of how Pr incorporation may influence the reducibility of the materials, and how the reducibility compares to the pure CeO₂ and Pr₆O₁₁. H₂-TPR was performed on the samples (Fig. 3); a study by Dolcetti and co-workers [35]. suggested the “real” redox properties of ceria can be studied by high temperature redox cycling, so temperature programmed reduction-oxidation-reduction (TPR-O-R) cycles were performed to further investigate the redox properties of ceria. Pure ceria (A) showed two reduction peaks, a broad low intensity peak at 500 °C and a more intense peak ca. 820 °C, representing the reduction of surface cerium species, and bulk CeO₂ to Ce₂O₃, respectively. In terms of H₂ consumption, little difference was observed between samples A and E, with H₂ consumption per gram of catalyst decreasing from 4.3 to 3.7 μmol_{H2} g⁻¹_{cat}; once normalised for surface area, this difference became more significant with values of 0.08 and 0.05 μmol_{H2} m⁻²_{cat} (Table S2). Sample F (CePrO₂) showed much enhanced reducibility, with 18.7 μmol_{H2} g⁻¹_{cat}; as this material had the lowest surface area of 28 m²/g, this corresponded to 0.67 μmol_{H2} m⁻²_{cat}, more than a magnitude of order greater than calculated for E. Interestingly, two low intensity peaks were observed in the low temperature region (< 650 °C) for sample E, whilst a single peak was observed for F, perhaps suggesting the presence of an additional phase in E. For comparison, the redox properties of Pr₆O₁₁ were analysed. A sharp reduction peak was observed at 490 °C, with no additional features observed. A significant increase in H₂ consumption was calculated for Pr₆O₁₁ in comparison with the other samples analysed, with a value of 90.4 μmol_{H2} g⁻¹_{cat} or 1.97 μmol_{H2} m⁻²_{cat} (Table S2). The reduction temperature observed for the

pure praseodymium oxide catalyst was in agreement with previously reported temperatures of phase transformations, suggesting the intense reduction peak may represent a phase change from Pr_6O_{11} to $\text{Pr}_x\text{O}_{2-x}$ [36, 37].

3.2 Catalyst Testing

The samples were tested as catalysts for the glycerol to methanol reaction, as described previously [13, 14]. Dilute glycerol was passed over a catalyst bed comprised of the samples diluted with SiC and heated to 360°C. The results of these reactions are summarised in Table 2 and full product selectivity is given in the supplemental information (Table S3 and S4). The glycerol conversion over sample **A**, **B** and **C** was high at > 97 %. Previously, we have reported a glycerol conversion of 84 % at this reaction temperature over a low surface area, commercially sourced ceria [13]. At this lower conversion, hydroxyacetone was the dominant product and the carbon mole selectivity to methanol was 7 %. We have observed that with increasing reaction temperature or catalyst surface area, the methanol selectivity is improved *via* cleavage of intermediate products, such as hydroxyacetone and ethylene glycol [14]. The addition of Zr to the ceria lattice resulted in a reduction of the methanol selectivity, however, the selectivity to hydroxyacetone and acetaldehyde increased from 6.4 and 8.7 to 13.0 and 11.0 % respectively over sample **C** (Table S3). We consider that acetaldehyde is formed from the radical cleavage of hydroxyacetone and from the radical cleavage of glycolaldehyde, an intermediate product from ethylene glycol [14]. The implication of this is that despite the greater surface area of samples **B** and **C**, the incorporation of Zr is detrimental to methanol selectivity. However, the greater carbon mass balance (*ca.* 10 %) has modestly improved the methanol space-time-yield from 97 $\text{g}_{\text{MeOH}} \text{kg}^{-1} \text{h}^{-1}$ over sample **A** compared to 102 $\text{g}_{\text{MeOH}} \text{kg}^{-1} \text{h}^{-1}$ over sample **C**. The lower CO_x concentration formed over **B** and **C** in the reaction mixture is a benefit of Zr incorporation. The relatively high carbon mole selectivity of CO_x over **A** of 13.1 % was reduced to 8.5 and 6.9 % over **B** and **C** respectively. The formation of CO_x is considered to originate from the conversion of alcohol and carboxylic acid products [14]. A modest increase in selectivity towards a number of by-products was also observed upon inclusion of Zr into the catalyst; acrolein, ethanol and acetic acid all showed increased selectivities over samples **B** and **C**, resulting in lower methanol selectivity. The concentration of unknown products over catalysts **A**, **B** and **C** of 24.9, 18.7 and 23.4 % respectively is relatively high compared to our previous results, which we reported to be *ca.* 15 % ceria [13]. The conversion of the lower surface area ceria we previously reported and tested at 360°C was found to be 84 % with a high selectivity to hydroxyacetone (31.6%). We consider that this series of catalysts, with higher surface areas can convert hydroxyacetone at this temperature and this results in a greater proportion of unidentified products. The unidentified products are combined to generate a total unknown entry in Table S3 and S4. They were analysed by GC1 are combined from many small peaks, we predict that these form from condensation reactions for example and have no commercial standard to compare against. Their low individual concentration makes identification challenging by other analytical techniques. Presently, we are attempting to reduce the formation of these products through catalysts design, rather than identify them.

The decreasing crystallinity of the sample **A** to **B** to **C** or reduced crystallite size does not appear to influence the glycerol conversion greatly, however, differences can be seen when the methanol yield was normalised to surface area. The normalised space-time-yield over **A** was found to be 0.052 $\text{mmol}_{\text{MeOH}} \text{m}^{-2} \text{h}^{-1}$, which reduced to 0.032 and 0.029 $\text{mmol}_{\text{MeOH}} \text{m}^{-2} \text{h}^{-1}$ over **B** and **C**. The initial activation or dihydroxylation of glycerol can be considered to be influenced by Zr incorporation.

Pr incorporation in samples **E** and **F** did not result in high glycerol conversion, however, this is largely due to the surface area reduction observed with increasing Pr concentration. Sample **E** and **F** converted 91 and 76 % of the glycerol respectively at 360 °C. However, the methanol carbon mole selectivity was maintained at *ca.* 12 % when compared to sample **A** (see table S4 for full product distribution). As we have previously shown that methanol selectivity is strongly linked to glycerol conversion, a methanol selectivity of 12% at 76% conversion suggests higher methanol selectivity could be observed at increased conversion over sample **F**. The hydroxyacetone concentration over **E** and **F** is greater than that over sample **A**, however, this is expected due to the lower conversion. The increased ethylene glycol concentration formed over **F** in particular suggests that the formation of methanol is perhaps derived from this pathway over the hydroxyacetone pathway [14]. The

methanol space-time-yield generated over **F** is reduced when normalised to catalyst mass, however, as a function of surface area a significant improvement can be achieved. The formation rate of methanol over **A** was found to be 0.052 and over **F** this increases to 0.076 mmol_{MeOH} m⁻² h⁻¹.

Here the increased reducibility present as a result of Pr incorporation may direct the reaction pathway to the more favourable ethylene glycol route [14]. Theoretically, via this route two methanol molecules can be produced per glycerol molecule. Sample **F** has a lower cell volume, crystallite size and surface area when compared to the ceria sample **A**. This suggests that Pr⁴⁺ is the dominant form of Pr in the lattice. Raman spectroscopy indicated that the concentration of oxygen vacancies was relatively high, as the ratio of the F_{2g} to defect mode was close to 1:1. In this case, we consider that the surface area is not the primary metric by which determines the likely methanol selectivity. The incorporation of Pr requires further study to elucidate the origin of the surface area normalised methanol space-time-yield, which appears to be related to the defect density and reducibility above a certain value. However, the results suggest that either the increased reducibility or the presence of Pr ions in the solid solution can direct the reaction pathway in a different way to that over ceria. Over the pure Pr-oxide, sample **G**, the methanol formation rates were lower than that over **A**, despite the enhanced reducibility. The high quantity of oxygen vacancies present on sample **G** may rationalise the higher hydroxyacetone selectivity due to preferential activation of the primary alcohol on glycerol. Therefore, the combination of Pr and Ce in a solid solution can be considered to be advantageous with respect to the transformation of glycerol to methanol.

4. Conclusions

A series of catalyst samples were prepared using ceria as a basis, and incorporating Zr and Pr ions into the lattice. The influence of Zr ions was limited and no improvements in the space-time-yield of methanol as a function of surface area was observed. In the case of incorporating Pr, this measure of catalytic activity was improved with a relatively high substitution ratio. Sample **F** which had a ratio of Pr:Ce of 1.7:1 by SEM-EDX and a high defect density according to Raman spectroscopy had the highest methanol formation rate when normalised to surface area, 1.5 times greater than ceria (sample **A**). This preliminary result can potentially lead to more selective catalysts for methanol production and contribute to the circular economy through the valorisation of bio-diesel waste.

Acknowledgments

We thank Dr Thomas E. Davies for assistance with the SEM-EDX analysis.

Funding Statement

This research was funded by EPSRC; grant number EP/P033695/1.

Data Accessibility

Representative data sets, such as XRD and Raman spectroscopic measurements, and testing data can be accessed at <http://doi.org/10.17035/d.2020.0102336163>

Supplemental material can be found online.

Competing Interests

We declare we have no competing interests.

Authors' Contributions

JD, LS, MJD, SHT, DJW, GJH and NFD contributed to the conception and design, or acquisition of data, or analysis and interpretation of data. MJD, LS, GJH and NFD drafted the article and revised it critically for important intellectual content. NFD had final approval of the published version.

References

- [1] Ewanick, S. & Bura, R. 2010 1 - Hydrothermal pretreatment of lignocellulosic biomass. In *Bioalcohol Production* (ed. K. Waldron), pp. 3-23, Woodhead Publishing.
- [2] Chowdhury, R., Ghosh, S., Manna, D., Das, S., Dutta, S., Kleinsteuber, S., Sträuber, H., Kamrul Hassan, M., Kuittinen, S. & Pappinen, A. 2019 Hybridization of sugar-carboxylate-syngas platforms for the production of bio-alcohols from lignocellulosic biomass (LCB) – A state-of-the-art review and recommendations. *Energy Conversion and Management* **200**, 112111. (DOI:<https://doi.org/10.1016/j.enconman.2019.112111>).
- [3] Sattlewal, A., Agrawal, R., Bhagia, S., Das, P. & Ragauskas, A. J. 2018 Rice straw as a feedstock for biofuels: Availability, recalcitrance, and chemical properties. *Biofuels, Bioproducts and Biorefining* **12**, 83-107. (DOI:10.1002/bbb.1818).
- [4] Otera, J. 1993 Transesterification. *Chem. Rev. (Washington, D. C.)* **93**, 1449-1470. (DOI:10.1021/cr00020a004).
- [5] Stein, Y. S., Antal, M. J. & Jones, M. 1983 A study of the gas-phase pyrolysis of glycerol. *Journal of Analytical and Applied Pyrolysis* **4**, 283-296. (DOI:[https://doi.org/10.1016/0165-2370\(83\)80003-5](https://doi.org/10.1016/0165-2370(83)80003-5)).
- [6] Carretin, S., McMorn, P., Johnston, P., Griffin, K. & Hutchings, G. J. 2002 Selective oxidation of glycerol to glyceric acid using a gold catalyst in aqueous sodium hydroxide. *Chemical Communications*, 696-697. (DOI:10.1039/B201112N).
- [7] Katryniok, B., Paul, S., Capron, M. & Dumeignil, F. 2009 Towards the Sustainable Production of Acrolein by Glycerol Dehydration. *ChemSusChem* **2**, 719-730. (DOI:10.1002/cssc.200900134).
- [8] Bienholz, A., Schwab, F. & Claus, P. 2010 Hydrogenolysis of glycerol over a highly active CuO/ZnO catalyst prepared by an oxalate gel method: influence of solvent and reaction temperature on catalyst deactivation. *Green Chemistry* **12**, 290-295. (DOI:10.1039/B914523K).
- [9] Katryniok, B., Paul, S., Belliere-Baca, V., Rey, P. & Dumeignil, F. 2010 Glycerol dehydration to acrolein in the context of new uses of glycerol. *Green Chemistry* **12**, 2079-2098. (DOI:10.1039/c0gc00307g).
- [10] Haider, M. H., Dummer, N. F., Zhang, D. Z., Miedziak, P., Davies, T. E., Taylor, S. H., Willock, D. J., Knight, D. W., Chadwick, D. & Hutchings, G. J. 2012 Rubidium- and caesium-doped silicotungstic acid catalysts supported on alumina for the catalytic dehydration of glycerol to acrolein. *Journal of Catalysis* **286**, 206-213. (DOI:10.1016/j.jcat.2011.11.004).
- [11] Sun, D., Yamada, Y., Sato, S. & Ueda, W. 2017 Glycerol as a potential renewable raw material for acrylic acid production. *Green Chemistry* **19**, 3186-3213. (DOI:10.1039/C7GC00358G).
- [12] Haider, M. H., Dummer, N. F., Knight, D. W., Jenkins, R. L., Howard, M., Moulijn, J., Taylor, S. H. & Hutchings, G. J. 2015 Efficient green methanol synthesis from glycerol. *Nat. Chem.* **7**, 1028-1032. (DOI:10.1038/nchem.2345).
- [13] Smith, J. P., Smith, L., Dummer, F. N., Douthwaite, M., Willock, J. D., Howard, M., Knight, W. D., Taylor, H. S. & Hutchings, J. G. 2019 Investigating the Influence of Reaction Conditions and the Properties of Ceria for the Valorisation of Glycerol. *Energies* **12**. (DOI:10.3390/en12071359).
- [14] Smith, L. R., Smith, P. J., Mugford, K. S., Douthwaite, M., Dummer, N. F., Willock, D. J., Howard, M., Knight, D. W., Taylor, S. H. & Hutchings, G. J. 2019 New insights for the valorisation of glycerol over MgO catalysts in the gas-phase. *Catalysis Science & Technology* **9**, 1464-1475. (DOI:10.1039/C8CY02214C).
- [15] Shido, T. & Iwasawa, Y. 1992 Regulation of reaction intermediate by reactant in the water-gas shift reaction on CeO₂, in relation to reactant-promoted mechanism. *Journal of Catalysis* **136**, 493-503. (DOI:[https://doi.org/10.1016/0021-9517\(92\)90079-W](https://doi.org/10.1016/0021-9517(92)90079-W)).
- [16] Kašpar, J., Fornasiero, P. & Graziani, M. 1999 Use of CeO₂-based oxides in the three-way catalysis. *Catalysis Today* **50**, 285-298. (DOI:[https://doi.org/10.1016/S0920-5861\(98\)00510-0](https://doi.org/10.1016/S0920-5861(98)00510-0)).
- [17] Mamontov, E., Egami, T., Brezny, R., Koranne, M. & Tyagi, S. 2000 Lattice Defects and Oxygen Storage Capacity of Nanocrystalline Ceria and Ceria-Zirconia. *The Journal of Physical Chemistry B* **104**, 11110-11116. (DOI:10.1021/jp0023011).

- [18] Hori, C. E., Permana, H., Ng, K. Y. S., Brenner, A., More, K., Rahmoeller, K. M. & Belton, D. 1998 Thermal stability of oxygen storage properties in a mixed CeO₂-ZrO₂ system. *Applied Catalysis B: Environmental* **16**, 105-117. (DOI:[https://doi.org/10.1016/S0926-3373\(97\)00060-X](https://doi.org/10.1016/S0926-3373(97)00060-X)).
- [19] Reddy, B. M., Thrimurthulu, G. & Katta, L. 2011 Design of Efficient Ce_xM_{1-x}O_{2-δ} (M = Zr, Hf, Tb and Pr) Nanosized Model Solid Solutions for CO Oxidation. *Catalysis Letters* **141**, 572-581. (DOI:10.1007/s10562-010-0484-z).
- [20] Hernández, W. Y., Centeno, M. A., Romero-Sarria, F. & Odriozola, J. A. 2009 Synthesis and Characterization of Ce_{1-x}Eu_xO_{2-x/2} Mixed Oxides and Their Catalytic Activities for CO Oxidation. *The Journal of Physical Chemistry C* **113**, 5629-5635. (DOI:10.1021/jp8092989).
- [21] Reddy, B. M., Thrimurthulu, G., Katta, L., Yamada, Y. & Park, S.-E. 2009 Structural Characteristics and Catalytic Activity of Nanocrystalline Ceria-Praseodymia Solid Solutions. *The Journal of Physical Chemistry C* **113**, 15882-15890. (DOI:10.1021/jp903644y).
- [22] Buyukkilic, S., Kim, S. & Navrotsky, A. 2014 Defect Chemistry of Singly and Doubly Doped Ceria: Correlation between Ion Transport and Energetics. *Angewandte Chemie International Edition* **53**, 9517-9521. (DOI:10.1002/anie.201404618).
- [23] Deganello, F. & Martorana, A. 2002 Phase Analysis and Oxygen Storage Capacity of Ceria-Lanthana-Based TWC Promoters Prepared by Sol-Gel Routes. *Journal of Solid State Chemistry* **163**, 527-533. (DOI:<https://doi.org/10.1006/jssc.2001.9442>).
- [24] Bunluesin, T., Gorte, R. J. & Graham, G. W. 1997 CO oxidation for the characterization of reducibility in oxygen storage components of three-way automotive catalysts. *Applied Catalysis B: Environmental* **14**, 105-115. (DOI:[https://doi.org/10.1016/S0926-3373\(97\)00016-7](https://doi.org/10.1016/S0926-3373(97)00016-7)).
- [25] Balducci, G., Kašpar, J., Fornasiero, P., Graziani, M. & Islam, M. S. 1998 Surface and Reduction Energetics of the CeO₂-ZrO₂ Catalysts. *The Journal of Physical Chemistry B* **102**, 557-561. (DOI:10.1021/jp972400n).
- [26] Zamar, F., Trovarelli, A., de Leitenburg, C. & Dolcetti, G. 1995 CeO₂-based solid solutions with the fluorite structure as novel and effective catalysts for methane combustion. *Journal of the Chemical Society, Chemical Communications*, 965-966. (DOI:10.1039/C39950000965).
- [27] Rodriguez, J. A., Hanson, J. C., Kim, J.-Y., Liu, G., Iglesias-Juez, A. & Fernández-García, M. 2003 Properties of CeO₂ and Ce_{1-x}Zr_xO₂ Nanoparticles: X-ray Absorption Near-Edge Spectroscopy, Density Functional, and Time-Resolved X-ray Diffraction Studies. *The Journal of Physical Chemistry B* **107**, 3535-3543. (DOI:10.1021/jp022323i).
- [28] McBride, J. R., Hass, K. C., Poindexter, B. D. & Weber, W. H. 1994 Raman and x-ray studies of Ce_{1-x}RE_xO_{2-y}, where RE=La, Pr, Nd, Eu, Gd, and Tb. *Journal of Applied Physics* **76**, 2435-2441. (DOI:10.1063/1.357593).
- [29] Santos, V., Zeni, M., Bergmann, C. P. & Hohemberger, J. M. 2008 Correlation between thermal treatment and tetragonal/monoclinic nanostructured zirconia powder obtained by sol-gel process. *Reviews on Advanced Materials Science* **17**, 62-70.
- [30] Chen, L., Mashimo, T., Omurzak, E., Okudera, H., Iwamoto, C. & Yoshiasa, A. 2011 Pure Tetragonal ZrO₂ Nanoparticles Synthesized by Pulsed Plasma in Liquid. *The Journal of Physical Chemistry C* **115**, 9370-9375. (DOI:10.1021/jp111367k).
- [31] Luo, M.-F., Yan, Z.-L., Jin, L.-Y. & He, M. 2006 Raman Spectroscopic Study on the Structure in the Surface and the Bulk Shell of Ce_xPr_{1-x}O_{2-δ} Mixed Oxides. *The Journal of Physical Chemistry B* **110**, 13068-13071. (DOI:10.1021/jp057274z).
- [32] Mineshige, A., Taji, T., Muroi, Y., Kobune, M., Fujii, S., Nishi, N., Inaba, M. & Ogumi, Z. 2000 Oxygen chemical potential variation in ceria-based solid oxide fuel cells determined by Raman spectroscopy. *Solid State Ionics* **135**, 481-485. (DOI:[https://doi.org/10.1016/S0167-2738\(00\)00403-3](https://doi.org/10.1016/S0167-2738(00)00403-3)).
- [33] Singh, P. & Hegde, M. S. 2008 Controlled synthesis of nanocrystalline CeO₂ and Ce_{1-x}M_xO_{2-δ} (M=Zr, Y, Ti, Pr and Fe) solid solutions by the hydrothermal method: Structure and oxygen storage capacity. *Journal of Solid State Chemistry* **181**, 3248-3256. (DOI:<https://doi.org/10.1016/j.jssc.2008.08.018>).
- [34] Kosacki, I., Suzuki, T., Anderson, H. U. & Colomban, P. 2002 Raman scattering and lattice defects in nanocrystalline CeO₂ thin films. *Solid State Ionics* **149**, 99-105. (DOI:[https://doi.org/10.1016/S0167-2738\(02\)00104-2](https://doi.org/10.1016/S0167-2738(02)00104-2)).

- [35] Terribile, D., Trovarelli, A., de Leitenburg, C., Dolcetti, G. & Llorca, J. 1997 Unusual Oxygen Storage/Redox Behavior of High-Surface-Area Ceria Prepared by a Surfactant-Assisted Route. *Chemistry of Materials* **9**, 2676-2678. (DOI:10.1021/cm9702732).
- [36] Borchert, Y., Sonström, P., Wilhelm, M., Borchert, H. & Bäumer, M. 2008 Nanostructured Praseodymium Oxide: Preparation, Structure, and Catalytic Properties. *The Journal of Physical Chemistry C* **112**, 3054-3063. (DOI:10.1021/jp0768524).
- [37] Sonström, P., Birkenstock, J., Borchert, Y., Schilinsky, L., Behrend, P., Gries, K., Müller, K., Rosenauer, A. & Bäumer, M. 2010 Nanostructured Praseodymium Oxide: Correlation Between Phase Transitions and Catalytic Activity. *ChemCatChem* **2**, 694-704. (DOI:10.1002/cctc.200900311).

Tables

Table 1. Sample composition, BET surface area and crystallite size.							
Sample Name	Elemental Composition (preparative)	Composition /% (SEM-EDX)		BET surface area ^a /m ⁻² g ⁻¹	Crystallite size ^b /nm	Lattice dimensions ^c /Å	Cell volume /Å ³
		Ce	M (Zr or Pr)				
A	CeO ₂	100	-	56	13.2	5.42	159
B	Ce ₃ ZrO ₂	88.4	11.6	88	9.0	5.40	157
C	CeZrO ₂	52.9	47.1	106	7.2	5.40	158
D	ZrO ₂	-	100	84	11.8	3.60 (a, b) 5.14 (c)	67
E	Ce ₃ PrO ₂	65.4	34.6	75	8.0	5.43	161
F	CePrO ₂	36.9	63.1	28	8.2	5.41	158
G	Pr ₆ O ₁₁	-	100	46	10.5	5.47	164

^a Nitrogen adsorption at -196 °C; ^b estimated from Scherrer equation with the (111) reflection; ^c lattice dimension of cubic fluorite (Fm3m) a = b = c, α = β = γ (90°), tetragonal structure (P4₂/nmc) a = b, c, α = β = γ (90°).

Table 2. Glycerol conversion and product selectivity data and normalised catalyst activity.

Catalyst	C_{GLY} /%	Major product selectivity ^a { $Sp(x)$ } /carbon mol. %						Carbon Bal. { B_c } /%	Specific activity /mmol _{MeOH} h ⁻¹ m ⁻²	Intrinsic activity /g _{MeOH} h ⁻¹ Kg ⁻¹
		MeOH	HAce	AceA	2,3-BD	EG	CO _x ^b			
A	98.8	12.6	6.4	8.7	1.4	3.7	13.1	67	0.052	96.86
B	97.7	11.5	9.3	11.9	1.9	8.8	8.5	73	0.032	94.98
C	99.9	11.4	13.0	11.0	3.2	2.7	6.9	76	0.029	101.76
D	67.9	7.9	30.5	7.7	3.5	5.8	5.1	72	0.013	37.17
E	90.6	12.1	10.8	8.8	1.3	4.8	11.8	81	0.039	100.38
F	74.3	12.9	19.2	9.4	3.9	8.8	9.0	72	0.076	70.44
G	64.4	10.6	23.0	6.74	2.4	7.4	4.8	88	0.042	65.08

Reaction conditions; reaction temperature 360 °C, 50 wt.% Glycerol/water solution (1 mL/h), Ar flow rate 15 mL/min, ^a determined from GC analysis of products recovered over 3 h (for full product list see Table S1); MeOH = methanol, HAce = hydroxyacetone, AceA = acetylaldehyde, 2,3-BD = 2,3-butanedione, EG = ethylene glycol, ^b combined CO and CO₂ %,

Figures

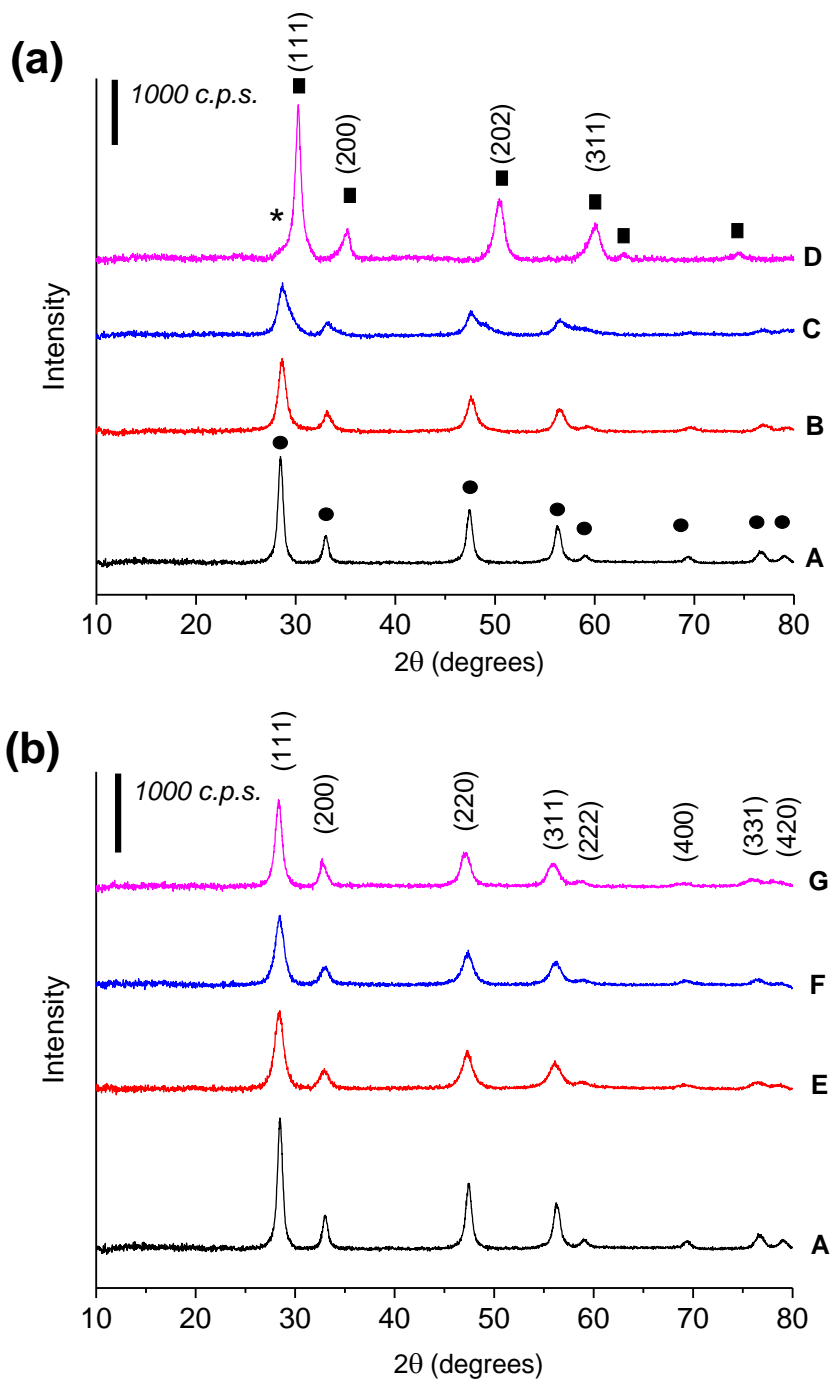


Figure 1. Powder XRD of ceria based samples; (a) samples with Zr, including ZrO₂ (D) and (b) samples with Pr, including Pr₆O₁₁ (G) compared to CeO₂ (A). ■ tetragonal structure (P4₂/nmc), * monoclinic impurity and ● cubic fluorite structure (Fm3m).

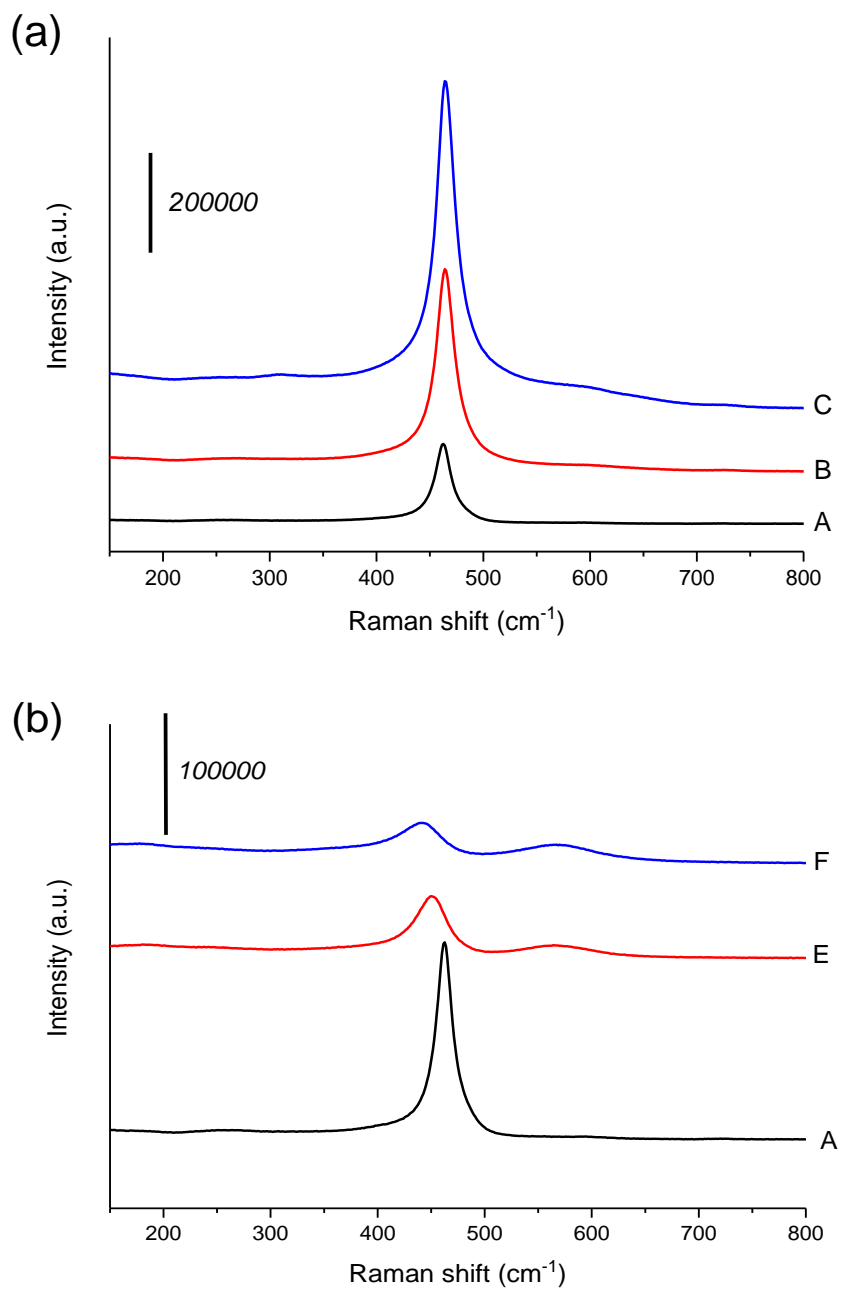


Figure 2. Raman spectroscopy of sample A (CeO₂) compared to those containing Zr (a) and Pr (b). Spectra of ZrO₂ and Pr₆O₁₁ see supplemental information.

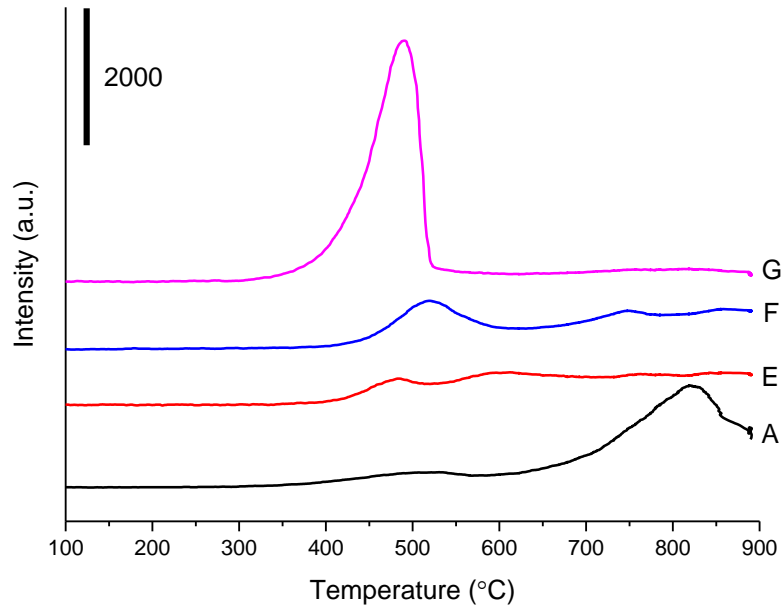


Figure 3. H₂-TPR profiles of samples E and F (Ce₃PrO₂ and CePrO₂) compared with CeO₂ (sample A) and Pr₆O₁₁ (sample G).